Efficient representation of mask transmittance functions for vectorial lithography simulations

Xinjiang Zhou, Chuanwei Zhang, Hao Jiang, Haiqing Wei, and Shiyuan Liu*

State Key Laboratory of Digital Manufacturing Equipment and Technology, Huazhong University of Science and Technology, Wuhan 430074, China
**Corresponding author: shyliu@mail.hust.edu.cn*

Received July 9, 2014; revised September 25, 2014; accepted September 29, 2014; posted October 3, 2014 (Doc. ID 216619); published October 28, 2014

In this paper, a generalized method to efficiently represent the incident-angle-dependent mask transmittance function (MTF) of a thick mask is proposed. This method expands the MTF into a series expansion, which consists of a set of predetermined basis functions weighted by a set of predetermined expansion coefficients. The predetermined basis functions are independent of the incident angles and thus may be computed offline and stored, while the expansion coefficients depend only on the incident angles and can be rapidly calculated online. Near-field and optical image simulations of thick masks have demonstrated the excellent accuracy and superior speed performance. © 2014 Optical Society of America

OCIS codes: (110.5220) Photolithography; (050.1960) Diffraction theory; (110.1758) Computational imaging.
http://dx.doi.org/10.1364/JOSAA.31.000B10

1. INTRODUCTION

Photomask optical proximity correction (OPC) and inverse lithography technology (ILT) have become indispensable for improving the performance of lithography processes [1–3]. Generally, an OPC or ILT process involves forward modeling known as lithography simulation and an inverse procedure, which aims to optimize the mask layout to minimize and compensate imaging distortion caused by optical proximity effects. Since the forward model is repeated many times in the inverse optimization algorithm, fast and accurate optical image simulation is highly desirable as one of the most critical components in the forward modeling simulations.

Abbe's and Hopkins' are two commonly used formulations of the optical imaging process for a partially coherent system [4–6]. Abbe's imaging formulation treats the source as consisting of a number of incoherent point sources, and the total optical image intensity is calculated as the superposition of all the optical image intensity distributions produced by these point sources. Hopkins' imaging theory formulates the imaging process through a fourfold integration with a kernel function called the transmission cross coefficient (TCC). Traditionally, the mask transmittance function (MTF) used in Abbe's and Hopkins' models has been assumed to be a binary mask consisting of "bright" areas with one value of transmittance and "dark" areas with another value of transmittance. This is known as the Kirchhoff thin mask approximation. Such a simplified approach of the MTF may be applicable as long as the width and length of the features are much larger than the illumination wavelength of the lithography system. However, the Kirchhoff assumption has become questionable in the most advanced lithography technology nodes as the feature size on a photomask is comparable with or even smaller than the illumination wavelength [7,8]. A more accurate thick mask model is needed to take into account the vector nature of the electromagnetic (EM) field and cope with incidence angles of illumination.

In principle, the MTF can be computed accurately using full-wave rigorous EM solvers including the finite-difference time-domain (FDTD) method [9,10], the rigorous coupled-wave analysis (RCWA) algorithm [11–13], and the waveguide (WG) method [14]. The FDTD method employs a direct temporal integration of the electromagnetic fields as described by Maxwell's equations. The RCWA and WG algorithms are frequency-domain methods using Fourier or waveguide-mode expansions for the EM field. There are also several approximation approaches, such as the geometrical theory of diffraction (GTD) [15,16], in which the total field scattered by an object is evaluated by adding a "fringe" field generated by electric and magnetic equivalent edge currents along the edges of the scattered to the physical optics (PO). Although able to improve the MTF accuracy, these thick mask solutions are generally time-consuming for image simulations because each solution incurs a high computational cost, is good for only one incident angle, and has to be repeated many times for different incident angles of a spatially extended source. Adam *et al.* [17] presented a hybrid Hopkins–Abbe (HHA) method that divides a source into sectors and associates each sector with a constant MTF. However, such a stepwise zeroth-order approximation lacks sufficient accuracy and it is tricky to sectorize a given practical source in a systematic and optimal fashion.

Recently, we proposed methods of cross triple correlation (CTC) [18] and convolution-variation separation (CVS) [19] to efficiently calculate the optical images for process variations. Following the same principle of the CTC and CVS methodologies, we propose in the present work a series expansion method for efficient representation and simulation of incident-angle-dependent MTFs. The key to the method is

 © 2014 Optical Society of America

to divide a spatially extended source into nonoverlapping radiating regions each consisting of multiple point sources, and associate to each radiating region an approximate MTF independent of the location of points within the same radiating region for the zeroth-order approximation. Going beyond the zeroth-order approximation, the MTF is represented by a series expansion which consists of a set of predetermined basis functions weighted by a set of expansion coefficients. The predetermined basis functions are independent of the incident angles and thus may be computed offline and stored, while the expansion coefficients depend only on the incident angles and can be rapidly calculated online.

The remaining of this paper is organized as follows. Section 2 presents the MTF representation method in optical lithography and then details the formulation of the MTF-based vectorial imaging process. Section 3 provides numerical results to demonstrate the higher accuracy and faster performance of the proposed method than the conventional EM solvers. Finally, we draw conclusions in Section 4.

2. THEORY

A. Representation of MTFs

Figure 1 illustrates the geometry of a mask pattern. We use two coordinate systems hereafter, a global coordinate (x, y, z) and a local coordinate $(e_\perp, e_\parallel)$ with $e_\perp$ and $e_\parallel$ denoting the directions of the transverse electric (TE) and transverse magnetic (TM) polarizations, respectively. Consider a monochromatic plane wave propagating in the direction of $\hat{k}$, where $\hat{k} = [\alpha, \beta, \gamma]^T$ is a vector of the direction cosines in the global coordinate. The incident plane wave is modulated by a thick mask and generates a field distribution just below the mask called the mask near-field. When we compute the actual mask near-field, it is convenient to use the spatial coordinate (x, y, z) system. The mapping between the two coordinate systems is

$$\begin{bmatrix} E_x \\ E_y \\ E_z \end{bmatrix} = \begin{bmatrix} -\frac{\beta}{\rho} & -\frac{\alpha\gamma}{\rho} \\ \frac{\alpha}{\rho} & -\frac{\beta\gamma}{\rho} \\ 0 & \rho \end{bmatrix} \begin{bmatrix} E_\perp \\ E_\parallel \end{bmatrix}, \tag{1}$$

where $\rho = \sqrt{\alpha^2 + \beta^2}$. E_x, E_y, and E_z are the electric field components along the x, y, and z axes, respectively; $E_\perp$ and $E_\parallel$ are the TE and TM components, respectively. Note that only two field components, e.g., E_x and E_y, are needed to uniquely specify a forward-propagating EM field

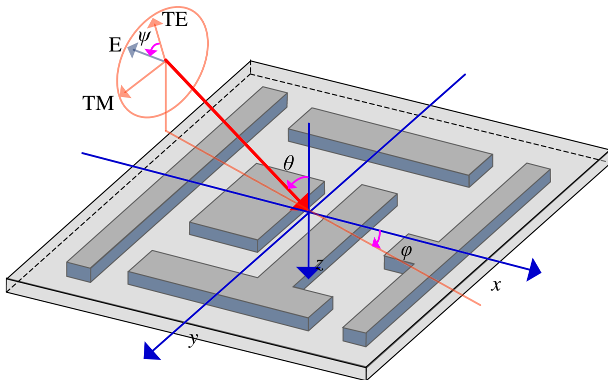

Fig. 1. Geometry of a thick mask pattern.

$$\begin{bmatrix} E_x \\ E_y \end{bmatrix} = T \begin{bmatrix} E_\perp \\ E_\parallel \end{bmatrix}, \tag{2}$$

where T is the 2×2 mapping matrix

$$T = \begin{bmatrix} -\frac{\beta}{\rho} & -\frac{\alpha\gamma}{\rho} \\ \frac{\alpha}{\rho} & -\frac{\beta\gamma}{\rho} \end{bmatrix}. \tag{3}$$

The third component E_z is determined by

$$E_z = -\frac{1}{\gamma}[\alpha E_x + \beta E_y]. \tag{4}$$

Consider a typical point source at (x_s, y_s) that emanates a monochromatic plane wave propagating in the direction of $\hat{k}_s = [\alpha_s, \beta_s, \gamma_s]^T$ with wave vector $\mathbf{k}_s = 2\pi[\alpha_s, \beta_s, \gamma_s]^T/\lambda$ and illuminates the thick mask, where λ is wavelength. The mask near-field from an incident plane wave TE mode is described by a 2×1 Jones vector $[u_{11}(\mathbf{x}; \mathbf{k}_s), u_{21}(\mathbf{x}; \mathbf{k}_s)]^T$ and that from a TM mode is described by a vector $[u_{12}(\mathbf{x}; \mathbf{k}_s), u_{22}(\mathbf{x}; \mathbf{k}_s)]^T$, where $\mathbf{x} = (x, y)$ is the spatial coordinate. For an incident plane wave with polarization vector $[E_\perp^s, E_\parallel^s]^T$ generated by a point source s, the mask near-field can be represented as

$$\mathbf{E}^{\text{mask}}(\mathbf{x}; \mathbf{k}_s) = \begin{bmatrix} E_\perp^{\text{mask}}(\mathbf{x}; \mathbf{k}_s) \\ E_\parallel^{\text{mask}}(\mathbf{x}; \mathbf{k}_s) \end{bmatrix} = U(\mathbf{x}; \mathbf{k}_s) T \begin{bmatrix} E_\perp^s \\ E_\parallel^s \end{bmatrix}, \tag{5}$$

where

$$U(\mathbf{x}; \mathbf{k}_s) = \begin{bmatrix} u_{11}(\mathbf{x}; \mathbf{k}_s) & u_{12}(\mathbf{x}; \mathbf{k}_s) \\ u_{21}(\mathbf{x}; \mathbf{k}_s) & u_{22}(\mathbf{x}; \mathbf{k}_s) \end{bmatrix} \tag{6}$$

is called the mask transfer matrix (MTM) with each element $u_{ij}(\mathbf{x}; \mathbf{k}_s)$ a scalar MTF. It is obvious that the scalar MTFs are dependent on both the spatial coordinate $\mathbf{x}$ and the incident angle $\mathbf{k}_s$.

A physical quantity being dependent on both a spatial coordinate and other parameters can be represented by a sum of multiple series expansion terms, with each term consisting of one function dependent only upon the spatial coordinate and another function dependent only upon the other parameters. Such a method of separation of variables has been employed in a variety of applications [20]. In the present context, each MTF $u_{ij}(\mathbf{x}; \mathbf{k}_s)$ or simply denoted as $u(\mathbf{x}; \mathbf{k}_s)$ with incident angle variations in Eq. (6) may be expanded into a Taylor series about the α_s and β_s at α_{0s} and β_{0s},

$$u(\mathbf{x}; \mathbf{k}_s) = \sum_{m \geq 0}^{M} \sum_{n \geq 0}^{N} (\alpha_s - \alpha_{0s})^m (\beta_s - \beta_{0s})^n \times u_{mn}^{\text{basis}}(\mathbf{x}; \mathbf{k}_{0s}) e^{[i2\pi(\alpha_s x + \beta_s y)/\lambda]}. \tag{7}$$

Here, $\mathbf{k}_0 = 2\pi[\alpha_{0s}, \beta_{0s}, \gamma_{0s}]^T/\lambda$ is a constant average wave vector for the radiating region, the basis MTFs $\{u_{mn}^{\text{basis}}(\mathbf{x}; \mathbf{k}_{0s})\}$ are dependent only on $\mathbf{x}$, while the mnth expansion coefficient $(\alpha_s - \alpha_{0s})^m (\beta_s - \beta_{0s})^n$ is dependent only on $\mathbf{k}_s$. The basis MTFs can be computed directly or obtained by numerical fitting. A set of MTFs corresponding to a set of different point sources in the radiating region of interest can be calculated with a rigorous EM solver such as the RCWA. Then, these calculated

MTFs provide constraints on the unknown basis MTFs. If the number of the calculated MTFs is equal to or larger than the number of the unknown basis MTFs, the basis MTFs can be solved using the least squares method. Note that it is rather important to factor out the "carrier" phase factor $\exp[i2\pi(\alpha_s x + \beta_s y)/\lambda]$, so that the remaining "envelope" becomes slow-varying as the incidence angle changes.

As shown in Eq. (7), the basis MTFs have been separated from the variable coefficients representing incident angles and need to be calculated only once. Using the precalculated basis MTFs, the MTFs under continuously changing incident angles can be calculated rapidly and accurately by summing up the series in Eq. (7). The basis MTFs remain constant and reusable so long as the mask layout and topography do not change. For the purpose of numerical calculation, all the equations need to be discretized into matrix and vector expressions, and the series in Eq. (7) should also be truncated to a finite series, which lead to approximation errors. Fortunately, due to the rapid convergence of the series, the truncation orders, denoted by M and N in Eq. (7), can usually be quite small.

B. Vectorial Lithography Modeling Based on MTFs

This section describes a vectorial imaging model of the optical lithography systems with the thick mask effect considered. Recognizing the fact that the oblique incidence effects can be naturally modeled using Abbe's imaging model, we discretize the spatially extended illumination source into point sources on a Cartesian grid. Each point source generates an oblique incident plane wave on the thick mask and produces a MTF, which in turn forms an image on the wafer after the projection lens. The total wafer image is a superposition of all the images produced by individual point sources. Figure 2 shows a typical vectorial imaging system, where the variables at the source side will have a subscript s, the mask side variables does not use subscript, and the image side variables use subscript $'$.

Two kinds of diffractions need to be considered in projection optics modeling. One is the diffraction from a flat screen to a spherical surface, and the other is its reversal, namely, the diffraction from a spherical surface to a flat surface near the focus. The former describes diffraction from the mask near-field to the entrance pupil of the projection lens in far-field, and the latter describes the focusing effect from the exit pupil to the wafer plane near the focus of the projection lens [21].

Once the mask near-field is known, the mask diffraction vector in (x, y, z) coordinate can be calculated by conducting the Fourier transform of the 2×1 mask near-field vector

$$\mathbf{E}^{\text{mask}}(\alpha, \beta; \mathbf{k}_s) = \mathbf{E}^{\text{mask}}(\mathbf{f}; \mathbf{k}_s) = \mathcal{F}\{\mathbf{E}^{\text{mask}}(\mathbf{x}; \mathbf{k}_s)\}, \tag{8}$$

where $\mathcal{F}$ is the Fourier transform, $\mathbf{f}$ represents the spatial frequency coordinate, and $\mathbf{f} = (f, g) = (\alpha/\lambda, \beta/\lambda)$. The diffraction to the entrance pupil, according to Fourier optics [22], can be described using the Huygens–Fresnel principle as

$$\mathbf{E}^{\text{ent}}(\alpha, \beta; \mathbf{k}_s) = \frac{\gamma}{j\lambda} \frac{e^{-ikr}}{r} \mathbf{E}^{\text{mask}}(\alpha, \beta; \mathbf{k}_s). \tag{9}$$

The field in wafer plane expressed in terms of the field at the exit pupil can be represented by a 2×1 vector matrix

$$\mathbf{E}^{\text{wafer}}(\alpha', \beta'; \mathbf{k}_s) = \frac{n'r'}{j\lambda\gamma'} e^{ik'r'} \mathbf{E}^{\text{ext}}(\alpha', \beta'; \mathbf{k}_s), \tag{10}$$

where $k = 2\pi n/\lambda$, $k' = 2\pi n'/\lambda$, n' is the reflection indices at the wafer side, $[\alpha, \beta, \gamma]^T$ and $[\alpha', \beta', \gamma']^T$ are the direction cosine of light propagation in the mask side and the wafer side, respectively, and r and r' are the radius of entrance pupil and exit pupil, respectively.

For a projection lens with transverse magnification R, according to the Abbe sine condition, the magnification scaling between the entrance and exit pupils is given as

$$\frac{\alpha}{n'\alpha'} = \frac{\beta}{n'\beta'} = R. \tag{11}$$

For an ideal lens, the conservation of energy requires that

$$|\mathbf{E}^{\text{ent}}(\alpha, \beta; \mathbf{k}_s)|^2 r^2 d\Omega = n' |\mathbf{E}^{\text{ext}}(\alpha', \beta'; \mathbf{k}_s)|^2 r'^2 d\Omega', \tag{12}$$

where the differential areas on each pupil are

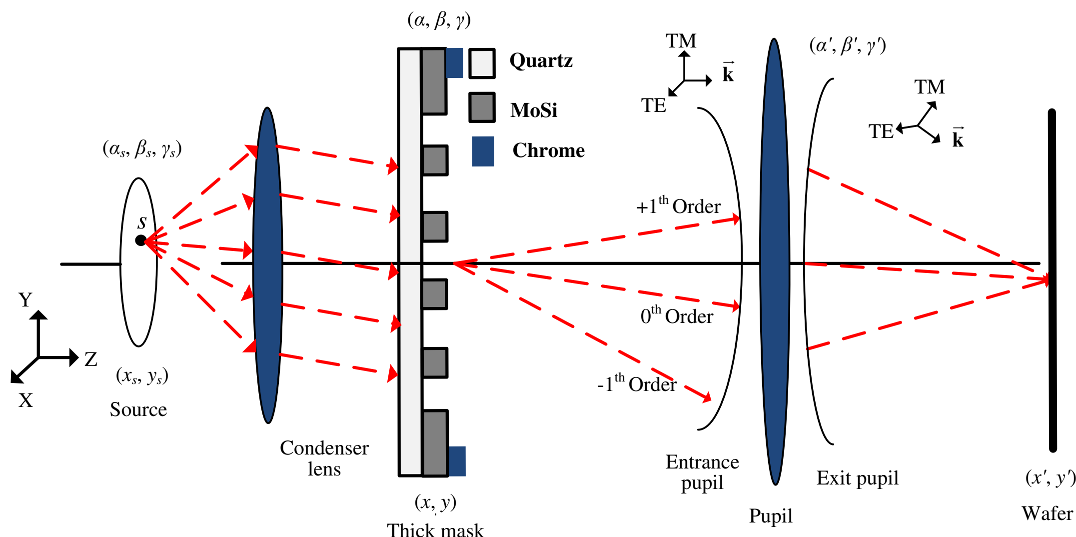

Fig. 2. Schematic of the vectorial imaging process in lithography systems.

$$d\Omega = \frac{d\alpha d\beta}{\gamma},$$
$$d\Omega' = \frac{d\alpha' d\beta'}{\gamma'}. \tag{13}$$

Substituting Eqs. (9)–(11), and (13) into Eq. (12) and ignoring the constant phase term, Eq. (12) translates to

$$|\mathbf{E}^{\text{wafer}}(\alpha', \beta'; \mathbf{k}_s)| = B(\gamma, \gamma')|\mathbf{E}^{\text{mask}}(\alpha, \beta; \mathbf{k}_s)|, \tag{14}$$

where

$$B(\gamma, \gamma') = \frac{n'}{R}\sqrt{\frac{n'\gamma}{\gamma'}}. \tag{15}$$

In practice, any projection lens has wavefront aberration and polarization aberration, and the image plane may not be exactly in focus. All these effects can be represented by a scalar function or a 2×2 vector matrix [23]. Equation (14) can be modified as

$$\mathbf{E}^{\text{wafer}}(\alpha', \beta'; \mathbf{k}_s) = B(\gamma, \gamma')P(\alpha', \beta')A(\alpha', \beta')\mathbf{V}(\alpha', \beta', \gamma') \times \Theta\mathbf{J}(\alpha', \beta')\Theta\mathbf{E}^{\text{mask}}(\alpha, \beta; \mathbf{k}_s), \tag{16}$$

where Θ denotes vectorial multiplication and $P(\alpha', \beta')$ is a low-pass filter function of projection lens

$$P(\alpha', \beta') = \begin{cases} 1, & \sqrt{\alpha'^2 + \beta'^2} \le \text{NA} \\ 0, & \text{otherwise} \end{cases}, \tag{17}$$

where $A(\alpha', \beta')$ is the wavefront aberration term, $\mathbf{J}(\alpha', \beta')$ is the polarization aberration term, and $\mathbf{V}(\alpha', \beta', \gamma')$ characterizes the rotating factor in a high numerical aperture (NA) projection lens when polarization light passes through the pupil [24,25]

$$\mathbf{V}(\alpha', \beta', \gamma') = \begin{vmatrix} V_{x\perp x} + V_{x\parallel x} & V_{y\perp x} + V_{y\parallel x} \\ V_{x\perp y} + V_{x\parallel y} & V_{y\perp y} + V_{y\parallel y} \\ V_{x\parallel z} & V_{y\parallel z} \end{vmatrix} = \begin{vmatrix} \frac{\beta'^2 + \alpha'^2\gamma'}{1-\gamma'^2} & \frac{\alpha'\beta'\gamma' - \alpha'\beta'}{1-\gamma'^2} \\ \frac{\alpha'\beta'\gamma' - \alpha'\beta'}{1-\gamma'^2} & \frac{\alpha'^2 + \beta'^2\gamma'}{1-\gamma'^2} \\ -\alpha' & -\beta' \end{vmatrix}. \tag{18}$$

The parameter $V_{p\perp q}$ or $V_{p\parallel q}$ (with $p, q = x$ or y) represents the vectorial field transformation from a p component projected onto the TE or TM polarization and then projected onto a q component at the image point. Consequently, the x, y, z components of the wafer field distribution in the spatial domain can be formulated as

$$\mathbf{E}_p^{\text{wafer}}(\mathbf{x}'; \mathbf{k}_s) = \mathbf{H}_p(\mathbf{x}', \mathbf{x}) \otimes \mathbf{E}_p^{\text{mask}}(\mathbf{x}; \mathbf{k}_s), \qquad p = x, y, z, \tag{19}$$

$$\mathbf{H}_p(\mathbf{x}', \mathbf{x}) = \mathcal{F}^{-1}[B(\gamma, \gamma')P(\alpha', \beta')A(\alpha', \beta') \times \mathbf{V}_p(\alpha', \beta', \gamma')\Theta\mathbf{J}_p(\alpha', \beta')], \tag{20}$$

where $E_p^{\text{mask}}(\mathbf{x}; \mathbf{k}_s)$ are the x, y, z components of the mask near-field $\mathbf{E}^{\text{mask}}(\mathbf{x}; \mathbf{k}_s)$ for each source radiating region. $\mathbf{H}_p(\mathbf{x}', \mathbf{x})$ is called the pupil function of the projection lens, $\mathcal{F}^{-1}$ denotes the inverse Fourier transform, and $\otimes$ denotes convolution. Then the optical image contributed by the point source s in the lth radiating region can be formulated as

$$I_l(\mathbf{x}'; \mathbf{k}_s) = \sum_{p=x,y,z} (\mathbf{H}_p \otimes \mathbf{E}_p^{\text{mask}})(\mathbf{H}_p \otimes \mathbf{E}_p^{\text{mask}})^*, \tag{21}$$

where $*$ denotes transposed conjugate.

According to Abbe's method, the subtotal optical image $I_l(\mathbf{x}')$ for the lth radiating region can be calculated as

$$I_l(\mathbf{x}') = \sum_s I_l(\mathbf{x}'; \mathbf{k}_s) = \sum_s \sum_{p=x,y,z} (\mathbf{H}_p \otimes \mathbf{E}_p^{\text{mask}})(\mathbf{H}_p \otimes \mathbf{E}_p^{\text{mask}})^*. \tag{22}$$

Substituting Eqs. (5)–(7) into Eq. (22), $I_l(\mathbf{x}')$ may be rewritten as

$$I_l(\mathbf{x}') = \sum_{m\ge 0}^{M} \sum_{n\ge 0}^{N} C_{l,mn} I_{l,mn}(\mathbf{x}'), \tag{23}$$

$$C_{l,mn} = \sum_s (\alpha_s - \alpha_{0s})^m (\beta_s - \beta_{0s})^n e^{[i2\pi(\alpha_s x + \beta_s y)/\lambda]}, \tag{24}$$

$$I_{l,mn}(\mathbf{x}') = \sum_{m'\ge 0}^{m} \binom{m}{m'} \sum_{n'\ge 0}^{n} \binom{n}{n'} \sum_{p=x,y,z} [\mathbf{H}_p \otimes \mathbf{E}_{p,(m-m')(n-n')}^{\text{mask}}(\mathbf{x}; \mathbf{k}_{0s})][\mathbf{H}_p \otimes \mathbf{E}_{p,m'n'}^{\text{mask}}(\mathbf{x}; \mathbf{k}_{0s})]^*. \tag{25}$$

Here, $\mathbf{E}_{p,mn}^{\text{mask}}(\mathbf{x}; \mathbf{k}_{0s}) = T u_{mn}^{\text{basis}}(\mathbf{x}; \mathbf{k}_{0s})[E_\perp^s, E_\parallel^s]^T$ is called the mnth basis mask near-field for the x, y, z polarization states of the lth radiating region, $I_{l,mn}(\mathbf{x}')$ is the mnth basis image of the lth radiating region that is independent of incident angles and thus may be computed offline and stored in advance, while the expansion coefficients $C_{l,mn}$ depend only on the incident angles and can be rapidly calculated online.

Finally, we can obtain the total optical image $I(\mathbf{x}')$ contributed by the entire source that contains all the nonoverlapping radiating regions as

$$I(\mathbf{x}') = \sum_l I_l(\mathbf{x}'). \tag{26}$$

The above derivation of light field transformations is good for a perfectly polarized illumination source or plane wave. In practice, an illumination source may be partially polarized or completely unpolarized. Without loss of generality, any polarization state of each source pixel, represented by a 2×2 density matrix, can be always diagonalized, namely, the polarization state can always be represented as an incoherent sum of two mutually orthogonal, perfectly polarized light fields. Consequently, the physical effects of any source pixel can be simulated as an incoherent combination of at most two perfectly polarized light fields.

The significance of Eqs. (23)–(26) is that the fixed mask-pupil convolutions are fully separated from the variable

coefficients representing the incident angles and can be precomputed, so that the optical image under a large range of incident angle variations can be quickly calculated. If N_s is the number of the discrete sampling points for a radiating region, a rigorous EM solver such as the RCWA needs to generate N_s sets of MTFs. Each MTF may be convolved with a pupil function and the convolution result may be squared to yield an image. Let T_{MTF} denote the computational complexity (computing time) for simulating one MTF by the rigorous EM solver, T_{image} be the computational complexity for obtaining an image from the MTF, δT be the extra complexity for summing up the images from the N_s source sampling points, and $T_{rigorous}$ be the total computational complexity for simulating the subtotal optical image for the radiating region. It is usually the case that $\delta T \ll T_{image}$ and $\delta T \ll T_{MTF}$, and thus the following formula holds true for all rigorous EM solvers

$$T_{rigorous} = (T_{MTF} + T_{image}) \times N_s. \tag{27}$$

In contrast, the proposed method only needs to obtain a set of basis MTFs, and then the subtotal optical image for the radiating region is calculated from these basis MTFs. Let N_b denote the number of the basis MTFs used in Eqs. (22)–(26), and N_c denote the number of calculations by the rigorous EM solver such as the RCWA to directly compute or numerically fit these basis MTFs. Apparently, $N_b \le N_c$, and thus the complexity $T_{offline}$ for offline computing the N_b basis MTFs is

$$T_{offline} = T_{MTF} \times N_c, \tag{28}$$

and the complexity T_{online} for online simulating the subtotal optical image for the radiating region is

$$T_{online} = T_{image} \times N_b \times N_s. \tag{29}$$

Here, the extra complexity for summing up the series of Eq. (23) is neglected as it is much smaller than T_{image}. Consequently, the total complexity for the proposed method including the offline and online calculations would be

$$T_{proposed} = T_{offline} + T_{online} = T_{MTF} \times N_c + T_{image} \times N_b \times N_s. \tag{30}$$

It is usually the case that $T_{image} \ll T_{MTF}$ and $N_c \approx N_b \ll N_s$, leading to $T_{proposed} \ll T_{rigorous}$ and indicating the apparently superior scalability of the proposed method. In this case, the proposed method is particularly desirable as the online image simulation is much faster than the offline MTFs calculation, i.e., $T_{online} \ll T_{offline} \ll T_{rigorous}$.

3. NUMERICAL RESULTS

We performed numerical simulations by taking a CD = 45 nm periodic contact-hole attenuated phase shift mask (AttPSM) with 1:1 duty ratio for an example, but the proposed method is also suitable for nonperiodic thick masks. The phase absorber material of the thick mask in this simulation is assumed to be 68 nm MoSiON with the optical constants ($n = 2.343$, $k = 0.586$) to provide a 180° phase shift and 6% transmission [26]. The illumination source for the lithographic imaging system is set as a dipole configuration with $\sigma_{out}/\sigma_{in}/\varphi_0 = 0.8/0.6/30°$, the wavelength is $\lambda = 193$ nm, and the NA is set as 1.35. All the simulations are performed on a 3.46 GHz HPZ800 workstation installed with MATLAB on Windows 7 (64-bit). Considering the mask magnification factor R of the projection lens, the incident angle is defined as

$$\theta = \arcsin \frac{\sigma \mathrm{NA}}{R}, \tag{31}$$

where σ is the distance of the point source from the center of illumination source. The azimuth angle is defined as the angle between the f axis and the vector from the center of source to the point source, as shown in Fig. 3.

We divide the entire dipole source into four nonoverlapping radiating regions. By symmetry considerations in our example, we only need to calculate the basis MTFs of one region such as region 1, and the basis MTFs for other three regions are obtained immediately without additional computation. We discretize region 1 into $N_s = 10 \times 10 = 100$ point sources so that the simulation results by using a rigorous EM approach are sufficiently accurate and can act as a reference to evaluate the performance of the proposed method. The direction cosines α_{0s} and β_{0s} of the constant average wave vector in Eq. (7) for radiating region 1 are 0.239 and 0.131 rad, respectively, and their corresponding incident and azimuthal angles are $\theta = 13.7°$ and $\varphi = 7.5°$, respectively.

In the present work, the truncation orders of Eq. (7) are set as $M = 2$ and $N = 2$, thus the basis MTFs for each radiating region have 9 terms. However, since the values of two cubic terms and one quartic term of the basis MTFs are quite small and can be neglected, 6 basis MTFs up to the quadratic term are enough to simulate the optical image. We select 8 point sources from radiating region 1 and calculate their MTFs by our in-house-developed RCWA solver with truncation orders of the Rayleigh expansion for the RCWA solver as 8 [11–13]. This indicates that we set $N_b = 6$ and $N_c = 8$ in Eqs. (28)–(30). Then we obtain the 6 basis MTFs by solving a set of 8 equations with the least squares method. In the simulations, the diffraction orders calculated by the RCWA solver are in the local coordinate $(e_\perp, e_\parallel)$. We use a set of T matrices

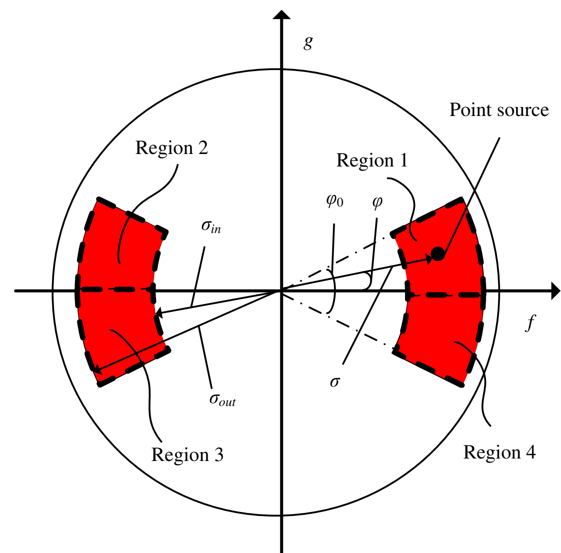

Fig. 3. Diagram of a dipole source configuration.

that depend on each individual diffraction order to map from the local coordinate $(e_{\perp}, e_{\parallel})$ to the global coordinate (x, y, z).

Once the basis MTFs in Eq. (7) are obtained offline, the MTFs and the mask near-field for an incident wave with any different incident angle can be calculated quickly. From Eqs. (5) and (6), the near-field x, y components $[E_x^{\mathrm{mask}}(\mathbf{x};\mathbf{k}_s), E_y^{\mathrm{mask}}(\mathbf{x};\mathbf{k}_s)]^T$ for a point source s with TE polarization are evaluated by $T[u_{11}(\mathbf{x};\mathbf{k}_s)E_{\perp}^s, u_{21}(\mathbf{x};\mathbf{k}_s)E_{\perp}^s]^T$. According to Eq. (7), the near-field can be expressed as

$$E_p^{\mathrm{mask}}(\mathbf{x};\mathbf{k}_s) = \sum_{m,n\geq 0}^{M,N} (\alpha_s - \alpha_{0s})^m (\beta_s - \beta_{0s})^n \times E_{p,mn}^{\mathrm{mask}}(\mathbf{x};\mathbf{k}_{0s}) e^{[i2\pi(\alpha_s x + \beta_s y)/\lambda]}. \tag{32}$$

Figures 4 and 5 depict simulation results for a source point with TE polarization in irradiating region 1 with $\alpha_s = 0.274$ rad and $\beta_s = 0.253$ rad, or $\theta = 15.7°$ and $\varphi = 14.5°$. It is obvious that $E_{p,mn}^{\mathrm{mask}}(\mathbf{x};\mathbf{k}_{0s})$ and $\mathbf{E}_p^{\mathrm{mask}}(\mathbf{x};\mathbf{k}_s)$ are complex values due to the fact that the MTF function has different "carrier" phase factors for different incident angles. Figures 6 and 7 show simulation results for a source point with TM polarization in irradiating region 1 with $\alpha_s = 0.235$ rad and $\beta_s = 0.112$ rad, or $\theta = 13.5°$ and $\varphi = 6.4°$. The near-fields for the point source s with TM polarization are evaluated by $T[u_{12}(\mathbf{x};\mathbf{k}_s)E_{\parallel}^s, u_{22}(\mathbf{x};\mathbf{k}_s)E_{\parallel}^s]^T$. From Figs. 4–7, it is clear that the x and y components of the mask near-field are decomposed into different terms, with each term associated directly to its corresponding basis MTFs. The sum of these terms gives an approximation result of the total mask near-field, and this is the fundamental principle behind the proposed method. If we define the error as a normalized difference between the result obtained by the proposed method and that by the rigorous EM solver, we can observe from Figs. 4–7 that it suffices to achieve the error of the order of 10^{-3} by truncating the series in Eq. (7) up to the quadratic term.

To further demonstrate the accuracy of the proposed method, the optical image of the CD = 45 nm thick mask is calculated based on Eqs. (23)–(26). For the source as shown in Fig. 3, as described above, only $N_c = 8$ times of RCWA calculations are enough to calculate the $N_b = 6$ basis MTFs. The refractive index at the image side is set as 1.4, the magnification factor R of the projection lens is set as 4, and the dipole source is set as TE polarization. For simplicity, no defocus and lens aberration are considered. Figure 8 shows simulation results of the total optical image $I(\mathbf{x}')$ and its decomposition into different terms

$$I_{mn} = \sum_l C_{l,mn} I_{l,mn}(\mathbf{x}'), \tag{33}$$

which are normalized by the largest intensity. Compared to the result obtained by $N_s = 100$ times of RCWA calculations, the normalized optical image error by the proposed method is of the order of 10^{-3}. The model accuracy is also characterized by evaluating the CD errors of 32 and 45 nm through-pitch test patterns at best focus condition. The through-pitch test patterns used in this simulation are typical lithography patterns that are basically one dimensional line-to-space patterns with constant CDs and varying spaces. The photoresist effect is approximated by a hard threshold represented by a dashed line, whose value is selected such that the CD is at the largest pitch.

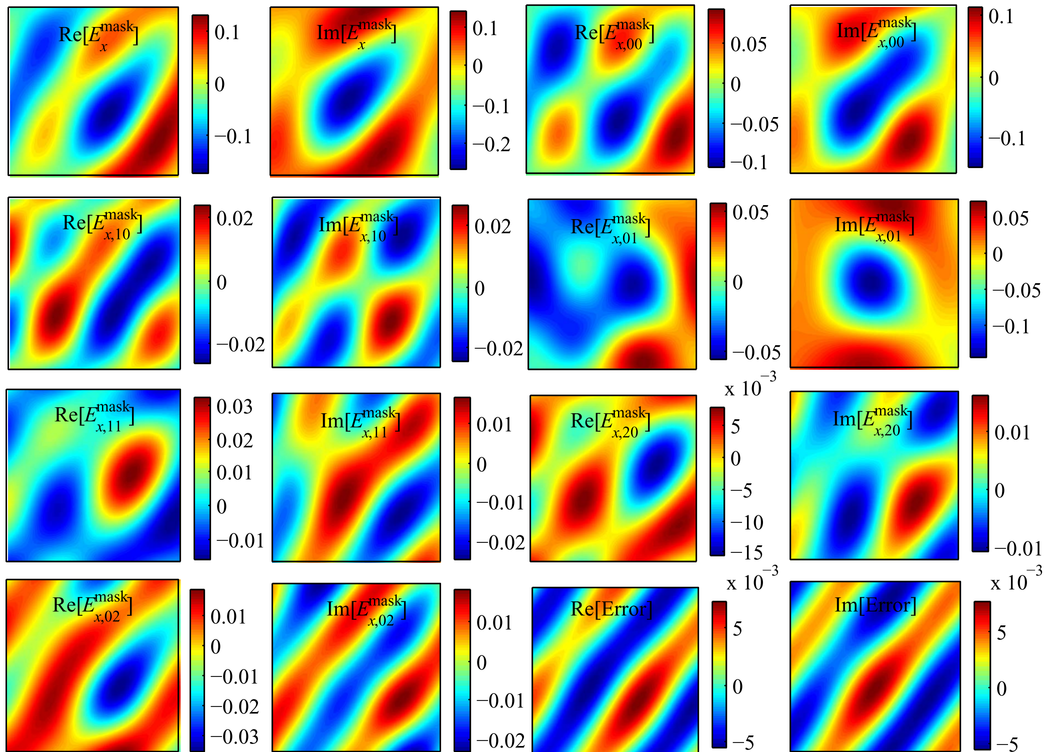

Fig. 4. Simulation results of the near-field x component $E_x^{\mathrm{mask}}(\mathbf{x};\mathbf{k}_s)$ and its decomposition into different terms $E_{x,mn}^{\mathrm{mask}}(\mathbf{x};\mathbf{k}_{0s})$ for a TE-polarization point source with incident and azimuthal angles as $\theta = 15.7°$ and $\varphi = 14.5°$. The mnth basis mask near-field $E_{x,mn}^{\mathrm{mask}}(\mathbf{x};\mathbf{k}_{0s})$ is calculated by the basis MTFs, and $E_x^{\mathrm{mask}}(\mathbf{x};\mathbf{k}_s)$ is calculated by summing all the basis mask near-fields. The normalized error between the result obtained by the proposed method and that by the rigorous EM solver is of the order of 10^{-3}.

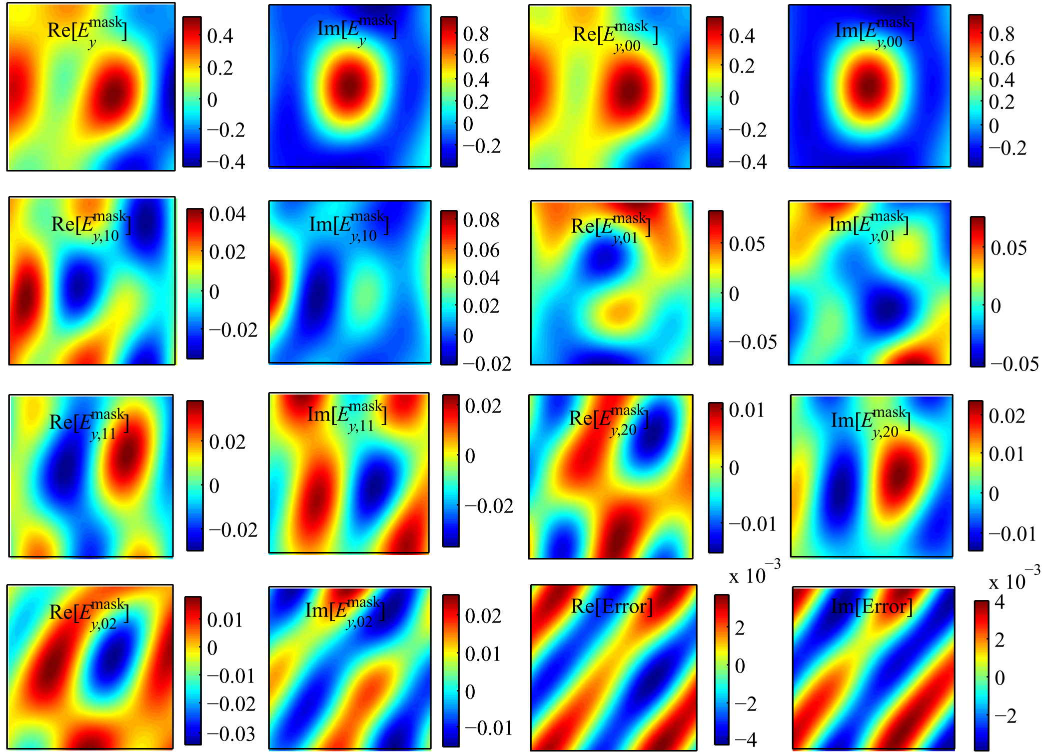

Fig. 5. Simulation results of the near-field $E_y^{\mathrm{mask}}(\mathbf{x};\mathbf{k}_s)$ and its decomposition into different terms $E_{y,mn}^{\mathrm{mask}}(\mathbf{x};\mathbf{k}_{0s})$ for a TE-polarization point source with incident and azimuthal angles as $\theta = 15.7°$ and $\varphi = 14.5°$. The mnth basis mask near-field $E_{y,mn}^{\mathrm{mask}}(\mathbf{x};\mathbf{k}_{0s})$ is calculated by the basis MTFs, and $E_y^{\mathrm{mask}}(\mathbf{x};\mathbf{k}_s)$ is calculated by summing all the basis mask near-fields. The normalized error between the result obtained by the proposed method and that by the rigorous EM solver is of the order of 10^{-3}.

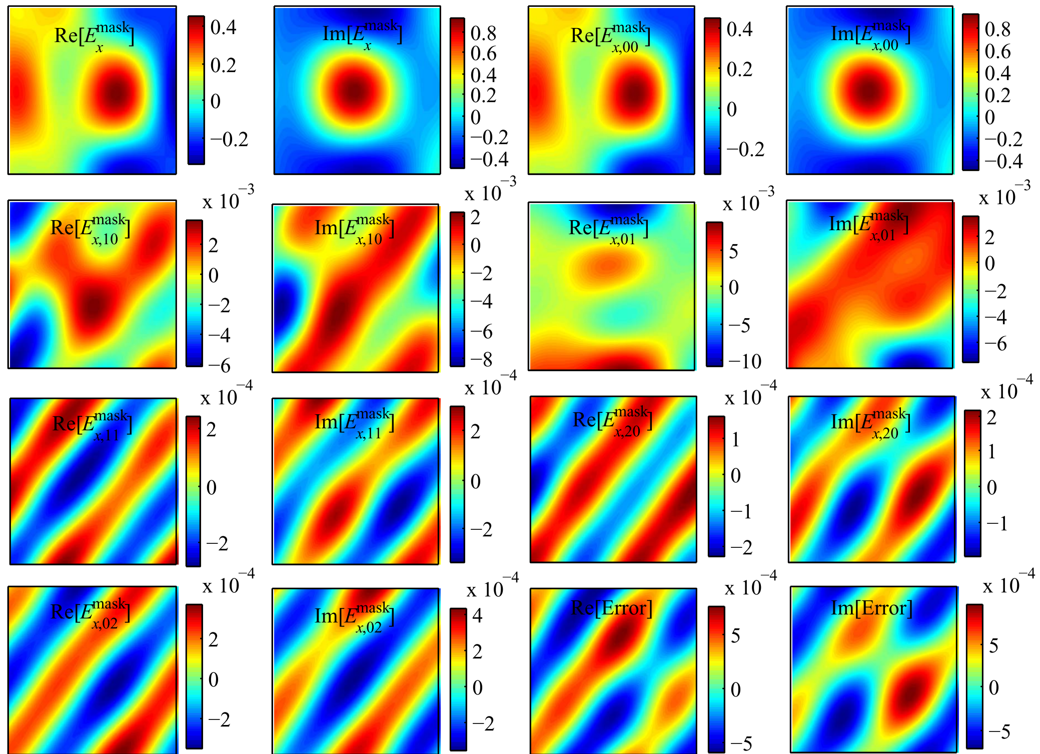

Fig. 6. Simulation results of the near-field $E_x^{\mathrm{mask}}(\mathbf{x};\mathbf{k}_s)$ and its decomposition into different terms $E_{x,mn}^{\mathrm{mask}}(\mathbf{x};\mathbf{k}_{0s})$ for a TM-polarization point source with incident and azimuthal angles as $\theta = 13.5°$ and $\varphi = 6.4°$. The mnth basis mask near-field $E_{x,mn}^{\mathrm{mask}}(\mathbf{x};\mathbf{k}_{0s})$ is calculated by the basis MTFs, and $E_x^{\mathrm{mask}}(\mathbf{x};\mathbf{k}_s)$ is calculated by summing all the basis mask near-fields. The normalized error between the result obtained by the proposed method and that by the rigorous EM solver is of the order of 10^{-3}.

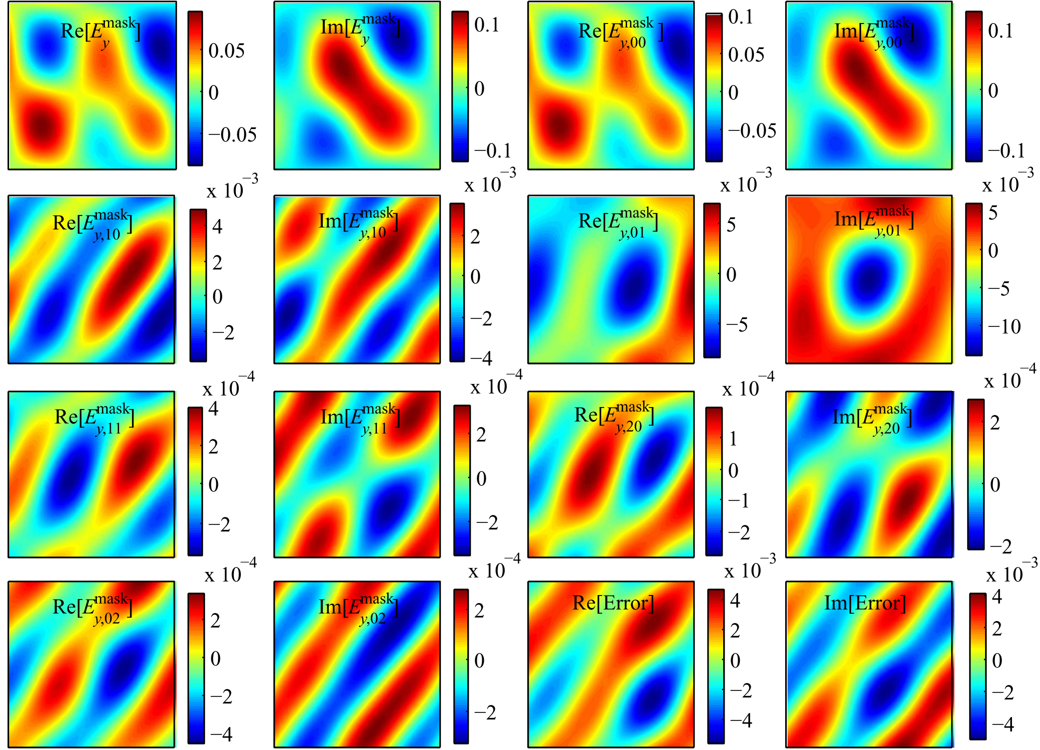

Fig. 7. Simulation results of the near-field $E_y^{\text{mask}}(\mathbf{x};\mathbf{k}_s)$ and its decomposition into different terms $E_{y,mn}^{\text{mask}}(\mathbf{x};\mathbf{k}_{0s})$ for a TM-polarization point source with incident and azimuthal angles as $\theta = 13.5°$ and $\varphi = 6.4°$. The mnth basis mask near-field $E_{y,mn}^{\text{mask}}(\mathbf{x};\mathbf{k}_{0s})$ is calculated by the basis MTFs, and $E_y^{\text{mask}}(\mathbf{x};\mathbf{k}_s)$ is calculated by summing all the basis mask near-fields. The normalized error between the result obtained by the proposed method and that by the rigorous EM solver is of the order of 10^{-3}.

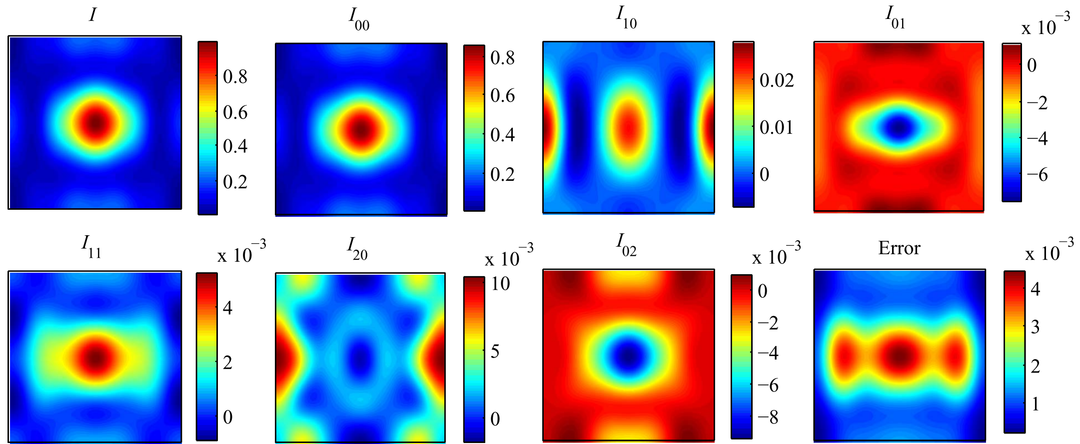

Fig. 8. Simulation results of the optical image intensity and its decomposition into different image terms $I_{mn} = \sum_l C_{l,mn} I_{l,mn}(\mathbf{x}')$ by using the proposed method. The mnth basis image $I_{l,mn}(\mathbf{x}')$ is calculated by the basis mask near-field, and $I(\mathbf{x}')$ is calculated by summing all the image terms I_{mn}. The normalized error between the result obtained by the proposed method and that by the rigorous EM solver is of the order of 10^{-3}.

As shown in Fig. 9, the CDs calculated using the proposed method are very close to the CDs calculated by the rigorous RCWA solver with the CD errors less than 0.5 nm, indicating that the proposed method is sufficiently accurate for many practical applications.

We also compare the computational complexity of the proposed method with that of the rigorous EM approaches. We take the source shown in Fig. 3 and the thick mask described above as an example. In this simulation, region 1 of the dipole source is discretized into $N_s = 5 \times 5 = 25$ point sources, and the rigorous RCWA solver needs to generate and use 25 sets of MTFs. The cost of generating each MTF using the RCWA is $T_{\text{MTF}} = 4.1$ s, and that for yielding an optical image from each MTF is $T_{\text{image}} = 8.7 \times 10^{-4}$ s. Consequently, it totally costs $T_{\text{rigorous}} = (4.1 + 8.7 \times 10^{-4}) \times 25 = 102.5$ s to produce the subtotal optical image for region 1. In contrast, it only costs $T_{\text{offline}} = 4.1 \times 8 = 32.8$ s of offline calculation time using the proposed method to obtain $N_b = 6$ basis MTFs by performing $N_c = 8$ times of RCWA calculations. In particular, the online simulation time to obtain the subtotal optical image for region

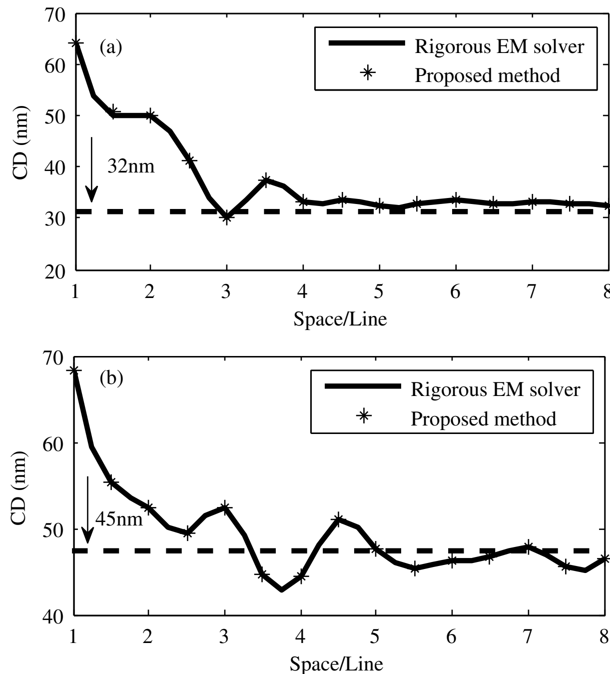

Fig. 9. CDs calculated by the rigorous EM solver and by the proposed method for (a) CD = 32 nm and (b) CD = 45 nm line-to-space patterns.

1 is even shorter, with a value of $T_{\mathrm{online}} = 8.7 \times 10^{-4} \times 6 \times 25 = 0.13$ s, indicating that the total time $T_{\mathrm{proposed}} = 32.8 + 0.13 = 32.93$ s using the proposed method is much shorter than that using the rigorous RCWA solver. Moreover, if region 1 of the dipole source is discretized into $N_s = 10 \times 10 = 100$ point sources to achieve more accurate results, the speed advantage is more obvious, with $T_{\mathrm{proposed}} = 32.8 + 0.52 = 33.32$ s in contrast to $T_{\mathrm{rigorous}} = (4.1 + 8.7 \times 10^{-4}) \times 100 = 410.1$ s. The superior scalability of the proposed method is thus confirmed.

4. CONCLUSION

In this paper, an incident-angle-dependent thick mask model has been proposed and demonstrated to enable fast thick mask simulations without serious loss of accuracy. The proposed efficient representation of MTFs for the vectorial lithography model is easy to implement and yields superior performance in optical image simulations.

ACKNOWLEDGMENTS

This work was funded by the National Natural Science Foundation of China (Grant Nos. 51475191 and 51405172), the Specialized Research Fund for the Doctoral Program of Higher Education of China (Grant No. 20120142110019), the National Science and Technology Major Project of China (Grant No. 2012ZX02701001), and the Program for Changjiang Scholars and Innovative Research Team in University of China.

REFERENCES

1. A. K. K. Wang, *Resolution Enhancement Techniques in Optical Lithography* (SPIE, 2001).
2. A. Poonawala and P. Milanfar, “Mask design for optical microlithography—an inverse imaging problem,” IEEE Trans. Image Process. **16**, 774–788 (2007).
3. D. O. S. Melville, A. E. Rosenbluth, A. Waechter, M. Millstone, J. Tirapu-Azpiroz, K. Tian, K. Lai, T. Inoue, M. Sakamoto, K. Adam, and A. Tritchkov, “Computational lithography: exhausting the resolution limits of 193-nm projection lithography systems,” J. Vac. Sci. Technol. B **29**, 06FH04 (2011).
4. A. K. K. Wang, *Optical Imaging in Projection Microlithography* (SPIE, 2005).
5. H. H. Hopkins, “On the diffraction theory of optical images,” Proc. R. Soc. London Ser. A **217**, 408–432 (1953).
6. M. Born and E. Wolf, *Principles of Optics*, 7th ed. (Pergamon, 1999).
7. A. Erdmann, G. Citarella, P. Evanschitzky, H. Schermer, V. Philipsen, and P. D. Bisschop, “Validity of Hopkins approximation in simulations of hyper NA (NA > 1) line-space structures for an attenuated PSM mask,” Proc. SPIE **6154**, 61540G (2006).
8. D. Flagello, B. Geh, S. Hansen, and M. Totzeck, “Polarization effects associated with hyper-numerical-aperture (>1) lithography,” J. Microlithogr. Microfabr. Microsyst. **4**, 031104 (2005).
9. A. Taflove, *Computational Electrodynamics: The Finite-Difference Time-Domain Method* (Artech House, 1995).
10. A. K. Wong and A. R. Neureuther, “Mask topography effects in projection printing of phase–shifting masks,” IEEE Trans. Electron Devices **41**, 895–902 (1994).
11. M. G. Moharam, D. A. Pommet, E. B. Grann, and T. K. Gaylord, “Stable implementation of the rigorous coupled-wave analysis for surface-relief gratings: enhanced transmittance matrix approach,” J. Opt. Soc. Am. A **12**, 1077–1086 (1995).
12. L. Li, “Formulation and comparison of two recursive matrix algorithms for modeling layered diffraction gratings,” J. Opt. Soc. Am. A **13**, 1024–1035 (1996).
13. S. Liu, Y. Ma, X. Chen, and C. Zhang, “Estimation of the convergence order of rigorous coupled-wave analysis for binary gratings in optical critical dimension metrology,” Opt. Eng. **51**, 081504 (2012).
14. K. D. Lucas, K. H. Tanabe, and A. J. Strojwas, “Efficient and rigorous three-dimensional model for optical lithography simulation,” J. Opt. Soc. Am. A **13**, 2187–2199 (1996).
15. A. Khoh, G. S. Samudra, W. Yihong, T. Milster, and B.-I. Choi, “Image formation by use of the geometrical theory of diffraction,” J. Opt. Soc. Am. A **21**, 959–967 (2004).
16. T. T. Elazhary, A. H. Morshed, and D. Khaill, “Modeling the field diffracted from photo mask at oblique incidence,” Appl. Opt. **49**, 4207–4216 (2010).
17. K. Adam, M. C. Lam, N. Cobb, and O. Toublan, “Application of the hybrid Hopkins–Abbe method in full-chip OPC,” Microelectron. Eng. **86**, 492–496 (2009).
18. S. Liu, W. Liu, and T. Zhou, “Fast algorithm for quadratic aberration model in optical lithography based on cross triple correlation,” J. Micro/Nanolithogr. MEMS MOEMS **10**, 023007 (2011).
19. S. Liu, X. Zhou, W. Lv, S. Xu, and H. Wei, “Convolution-variation separation method for efficient modeling of optical lithography,” Opt. Lett. **38**, 2168–2170 (2013).
20. W. Miller, Jr., *Symmetry and Separation of Variables* (Cambridge University, 1984).
21. D. Peng, P. Hu, V. Tolani, T. Dam, J. Tyminski, and S. Slonaker, “Toward a consistent and accurate approach to modeling projection optics,” Proc. SPIE **7640**, 76402Y (2010).
22. J. Goodman, *Introduction to Fourier Optics* (McGraw-Hill Science, 1996).
23. K. Lai, A. E. Rosenbluth, G. Han, J. Tirapu-Azpiroz, J. Meiring, A. Goehnermeier, B. Kneer, M. Totzeck, L. Winter, W. Boeij, and M. Kerkhof, “Modeling polarization for hyper-NA lithography tools and masks,” Proc. SPIE **6520**, 65200D (2007).
24. D. G. Flagello, “High numerical aperture imaging in homogeneous thin films,” Ph.D. dissertation (University of Arizona, 1993).
25. D. G. Flagello, T. Milster, and A. E. Rosenbluth, “Theory of high-NA imaging in homogeneous thin films,” J. Opt. Soc. Am. A **13**, 53–64 (1996).
26. A. Erdmann and P. Evanschitzky, “Rigorous electromagnetic field mask modeling and related lithographic effects in the low k1 and ultrahigh numerical aperture regime,” J. Micro/Nanolithogr. MEMS MOEMS **6**, 031002 (2007).